EXPERIMENTAL PERFORMANCE EVALUATION OF AN ORC IN A CHEST-LIKE CARNOT BATTERY

Robin Tassenoy[1]*, Kenny Couvreur[1], Michel De Paepe[1,2], Steven Lecompte[1,2]

[1]Department of ElectroMechanical, Systems and Metal Engineering, Ghent University, Ghent, Belgium

[2]FlandersMake@UGENT, Core lab EEDT-MP, Leuven, Belgium

*Corresponding Author: Robin.Tassenoy@UGent.be

ABSTRACT

Due to the continuously increasing share of renewables in the power mix, large-scale energy storage systems are becoming essential to ensure secure and stable energy supply. Carnot batteries, a combination of a power-to-heat, a thermal storage and a heat-to-power system, could potentially provide a solution. In literature, the Compressed Heat Energy Storage (CHEST) concept has been introduced as a Carnot battery subset. Using both sensible and latent thermal storage, it optimizes the temperature profiles between the charging- and discharging cycle and the thermal storage system. Despite promising theoretical results, the concept was never demonstrated until recently. A first of its kind CHEST Carnot battery was developed within the European Horizon2020 project CHESTER. It consists of a high temperature heat pump which charges a thermal storage system and an organic Rankine cycle (ORC) that discharges the storage. The storage system is composed of a latent heat part, using a phase change material with a melting temperature around 133 °C and a sensible heat part with pressurized water. In this paper, the interaction between the thermal storage system and the ORC is studied. Specifically, the influence of the heat distribution over the sensible and latent storage on the ORC operation is investigated. The results show that the thermal efficiency of the ORC is not sensitive to the actual distribution of the heat input, as long as the heat input to the system can be sustained. The ORC itself supports a high flexibility towards different residual heat source temperatures and storage systems, making it applicable in a wide range of operating scenarios.

1 INTRODUCTION

The share of renewables in the global power mix is continuously increasing, peaking at 30 % in 2022. In Europe, renewable electricity production even accounted for 43 % (Enerdata, 2023). Renewable energy technologies like wind and photovoltaic power hold potential to transform the fossil dominated energy system to a 100 % sustainable one (He et al., 2022). Large deployment of variable renewable energies (VRE) can thus be expected. However, these VRE can cause major problems to the stability of the electrical grid due to their intermittent nature. Energy storage is considered one of the main drivers to provide the flexibility required for full decarbonization of the electricity grid (European Commission et al., 2020).

Carnot batteries are an emerging electrical energy storage (EES) concept that may contribute to this decarbonization. The Carnot battery concept involves three steps. First, electrical energy is converted into heat using a heat pump or joule heater. Secondly, the heat is stored. Finally, a heat engine technology is used to convert the heat back to electricity when needed. Dumont et al. (Dumont et al., 2020) give an overview of the relevant performance indicators, different subcategories and the state-of-the-art experimental prototypes.

The CHEST concept is a Carnot battery subset which is characterized by latent heat thermal energy storage (LH-TES) using phase change materials (PCM), combined with a conventional Rankine cycle for charging- and discharging (Steinmann, 2014). The idea is to minimize the temperature differences between the working fluid and storage medium during phase change. By using sensible thermal storage for subcooling (heat pump) or preheating (ORC), an optimal match between the storage and cycle

https://doi.org/10.52202/077185-0049

temperature profile can be created. Steinmann suggested a multi-stage charging cycle with ammonia or water as working fluid, combined with sensible and latent heat storage between 200 and 400 °C. Jockenhöfer et al. (Jockenhöfer et al., 2018) adapted this concept to work with low temperature thermal integration. The use of residual heat omits the need for multiple compression stages and significantly reduces the cycle complexity, while improving the overall round-trip efficiency of the system. In this simplified concept, sensible storage and a LH-TES with phase change temperature of 133 °C are used.

The European Horizon 2020 project CHESTER focused on further development of the CHEST storage concept and its integration in the heat- and electricity sector (CHESTER, 2023). Within the project, the CHEST concept was further optimized (Hassan et al., 2022; Hassan et al., 2020) and several use cases were identified (Lund, 2021; Lund et al., 2021; Sánchez-Canales et al., 2020; Stark & Bestenlehner, 2021; Vaz & Carrera, 2021). Given that the concept was never demonstrated experimentally (Dumont et al., 2020; Novotny et al., 2022; Vecchi et al., 2022), the project also developed the first CHEST laboratory prototype. Previous publications addressed the design, development and stand-alone testing of the separate subsystems: high temperature heat pump (HT-HP) (Hassan et al., 2019; Hassan et al., 2022), high-temperature thermal storage system (HT-TESS) (Weller et al., 2019) and organic Rankine cycle (ORC) (Couvreur et al., 2022; De Paepe et al., 2019).

After testing of the separate subsystems, they were integrated to form the full CHESTER-laboratory prototype of which a simplified flow diagram is given in Figure 1.

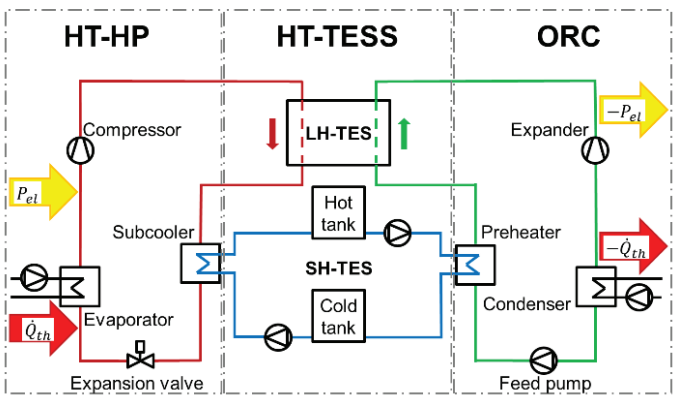

Figure 1: Simplified flow diagram of the CHESTER laboratory prototype (Theologou et al., 2024).

This paper discusses the full system discharging tests, with special attention towards the interaction between the HT-TESS, which consists of both latent heat (LH) and sensible heat (SH) thermal storage, and the ORC. Therefore it has two main research goals. First, it demonstrates the CHEST concept experimentally by performing discharging tests. Secondly, it studies the impact of division of heat input to the ORC over the LH- and SH-TES and thus experimentally assesses the match between the storage system and discharging cycle.

2 METHODOLOGY

2.1 Experimental prototype

A simplified overview of the full setup is shown in Figure 1. In this publication, focus is given to the HT-TESS and the ORC. As visualized, the HT-TESS has two main components: a two-tank sensible storage system (SH-TES) and a latent storage system (LH-TES). The SH-TES consists of two pressurized water tanks, while the LH-TES uses an eutectic mixture of 33 wt% $LiNO_3$ and 67 wt% KNO_3 with a theoretical phase change temperature of 133 °C. This eutectic mixture was not obtained perfectly, resulting in a melting temperature range from approximately 128 to 136 °C. The ORC uses R1336mzz(E) as working fluid, which has a critical pressure of 31.5 bar and a critical temperature of 137.7 °C.

https://doi.org/10.52202/077185-0049

During discharge, the water in the SH-TES is pumped from the hot to the cold tank through the ORC preheater, where it heats up the ORC working fluid. The preheated refrigerant is then pumped from bottom to top of the LH-TES through finned tubes where it evaporates. More information on the integration of the different subsystems and the complete prototype can be found in (Theologou et al., 2024). For a more detailed description of the HT-TESS the reader is referred to (Weller et al., 2019). A more detailed description of the ORC itself can be found in (Couvreur et al., 2022).

An example Ts-diagram of the ORC cycle is shown in Figure 2. The numbering in the diagram is detailed in Table 1 and will be used to discuss the results. All sensors have been integrated as received by the supplier. Therefore, the absolute measurement error indicated by the supplier is considered during the analysis.

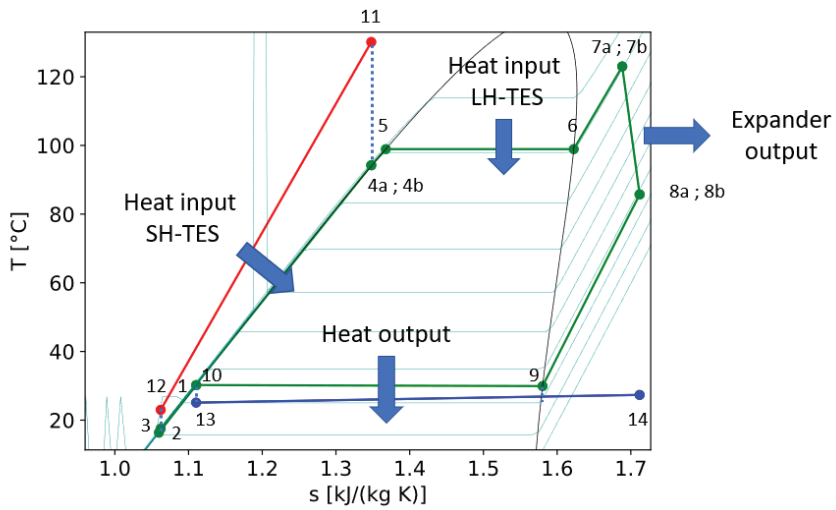

Figure 2: Ts-diagram of the ORC cycle. The red line indicates the SH-TES, the green lines make up the ORC cycle and the blue line is the condenser cold sink. The LH-TES temperature profile is not indicated on the figure.

Table 1: Overview of the measured variables.

Numbering	Description	Numbering	Description
1: T1 - P1	Condenser outlet	13: T13	Condenser cooling fluid inlet
2: T2 - P2	Pump inlet	14: T14	Condenser cooling fluid outlet
3: T3 - P3	Preheater inlet	15: T15	LTES – PCM temperature
4: T4a - P4a	Preheater outlet	$\dot{m}_r$	Refrigerant mass flow rate
4: T4b - P4b	Evaporator inlet	$\dot{m}_{ph,hf}$	Preheater heating fluid mass flow rate
7: T7a - P7a	Evaporator outlet	$\dot{m}_{cond,cf}$	Condenser cooling fluid mass flow rate
7: T7b - P7b	Expander inlet	N_{pump}	Pump speed
8: T8a - P8a	Expander outlet	$\dot{W}_{pump}$	Pumping power
8: T8b - P8b	Condenser inlet	N_{exp}	Expander speed
11: T11 - p11	Preheater heating fluid inlet	$\dot{W}_{pump}$	Expander power
12: T12 - p12	Preheater heating fluid outlet		

2.2 Test matrix

The influence of the heat source temperature, cold sink temperature, refrigerant mass flow rate, expander speed and expander internal volume ratio on the steady-state ORC operation was discussed

https://doi.org/10.52202/077185-0049

elaborately in a previous publication (Couvreur et al., 2022). In this work, this exhaustive evaluation is not repeated. An overview of the adopted target test parameters is provided in Table 2.

This work focuses on the interaction between the HT-TESS and the ORC. Therefore, the refrigerant mass flow rate ($\dot{m}_r$), the expander internal volume ratio and the expander speed (N_{exp}) were kept at their nominal values during all tests discussed. The refrigerant mass flow rate was chosen at the low end of the range tested previously, which corresponds with the lowest evaporation pressure for a given expander internal volume ratio and expander speed. As such, sufficient superheat can be maintained at the expander inlet for longer test periods, which maximizes the test duration. For similar reasons, the lowest internal volume ratio, corresponding to an expander valve position of 170 ° was used. Finally, an expander speed of 1000 RPM was selected as it results in high power output and expander isentropic efficiency, while avoiding system resonances occurring at lower speeds. The preconditioning of the SH-TES and the target subcooling at the evaporator inlet (point 4 in Figure 2) during operation have been varied. At the beginning of each discharging test, the HT-TESS is preconditioned. This means that the LH-TES and the hot tank of the SH-TES are heated up to the desired setpoint a priori. For given ORC parameters, the subcooling at the LH-TES evaporator inlet is regulated by controlling the water mass flow rate between the SH-TES tanks ($\dot{m}_{ph,hf}$). This mass flow rate is varied during the test to maintain a target subcooling.

Table 2: Overview of the initialization and operational parameter targets during the tests.

Test	T_{LH-TES} [°C]	T_{SH-TES} [°C]	N_{exp} [RPM]	$\dot{m}_r$ [kg/s]	SC_{target} [°C]
1	138	135	1000	0.373	5 - 10
2	138	120	1000	0.373	5 - 10
3	138	120	1000	0.373	15 - 20

2.3 Data reduction

The heat input to the ORC is split over the preheater and evaporator. The preheater heat input can be calculated based on the water side and the refrigerant side. In the LH-TES evaporator, only measurements at the refrigerant side are available. Therefore, all heat inputs are determined based on the refrigerant side, as shown in Equations (1) to (3). In some operating points the refrigerant may be partially evaporated at the preheater outlet. As a state in the two-phase region is not uniquely determined by the pressure and temperature, the heat input in the separate heat exchangers cannot be calculated accurately in that case. To avoid this problem, the total heat input can also be determined based on the state before the preheater (3) and after the evaporator (7a) directly.

$$\dot{Q}_{ph,in,r} = \dot{m}_r \,.\, (h_{4b} - h_3) \tag{1}$$

$$\dot{Q}_{ev,in,r} = \dot{m}_r \,.\, (h_{7a} - h_{4b}) \tag{2}$$

$$\dot{Q}_{in} = \dot{Q}_{ph,in,r} + \dot{Q}_{ev,in,r} = \dot{m}_r \,.\, (h_{7a} - h_3) \tag{3}$$

The expander is characterized by its isentropic and volumetric efficiency. The isentropic efficiency (η_{exp}) expresses how close the power generated by the actual expansion process approximates the power of an isentropic process as expressed by Equation (4).

$$\eta_{exp} = \frac{\dot{W}_{exp}}{\dot{W}_{exp,is}} \tag{4}$$

With:

$$\dot{W}_{exp,is} = \dot{m}_r \,.\, (h_{7b}(T_{7b}, p_{7b}) - h_{8a,is}(p_{8a}, s_{7b})) \tag{5}$$

Where: $s_{7b} = f(T_{7b}, p_{7b})$

The volumetric efficiency is another key parameter for the volumetric performance of positive displacement expanders and is evaluated as Equation (6):

https://doi.org/10.52202/077185-0049

$$\eta_{vol} = \frac{\dot{m}}{\dot{m}_{th}} \tag{6}$$

with $\dot{m}$ the actual measured mass flow rate and $\dot{m}_{th}$ theoretical mass flow rate admitted by the expander. The mass encountered in the cylinder at the end of the compression stroke is often neglected as it is typically small. In this case, the volumetric efficiency is calculated according to Equation (7):

$$\eta_{vol} = \frac{\dot{m}_{in}}{\frac{RPM}{60} \cdot \rho_{in} \cdot V_{ic}} \tag{7}$$

where ρ_{in} is the density at the expander inlet and V_{ic} the cylinder volume when the inlet valve closes.

The thermal cycle efficiency is defined as Eq. (8):

$$\eta_{cycle} = \frac{\dot{W}_{net}}{\dot{Q}_{in}} \tag{8}$$

The net amount of power generated by the ORC is:

$$\dot{W}_{net} = \left|\dot{W}_{exp}\right| - \dot{W}_{pump} \tag{9}$$

Comparing the ORC cycle efficiency to the theoretical maximum efficiency that can be reached with the cold and hot source present when assuming infinite heat capacity (i.e. the Carnot efficiency), results in a definition for the fraction of Carnot (FoC):

$$FoC = \frac{\eta_{cycle}}{\eta_{Carnot}} \tag{10}$$

With:

$$\eta_{Carnot} = 1 - \frac{T_{13}}{T_{7a}} \tag{11}$$

where both temperatures should be expressed in Kelvin. The hot temperature is defined based on the refrigerant flow (T_{7a}) instead of the secondary side, due to the complex evolution of the temperature field in the LH-TES. The temperature glide during the heat transfer is neglected. The highest temperature at each time instance is thus used, which results in a conservative estimate of the Carnot efficiency. The inlet temperature of the cooling fluid in the condenser (T_{13}) is used as cold temperature reference. In practice, the subcooler water inlet temperature is even lower. In the current prototype, this temperature is not measured and the degree of subcooling at the subcooler outlet (point 2 in Figure 2) is rather high for operational safety. The FoC could thus be improved with better control of the degree of subcooling. For these reasons, it is opted to express the Carnot efficiency based on the condenser water inlet temperature (T_{13}).

2.4 Quasi-steady state performance

The heat input to the ORC is inherently transient during operation with the LH-TES evaporator due to the changing state-of-charge (SOC) of the storage system. As the initial conditions and start-up procedure may vary in between different experiments, it is difficult to compare the instantaneous system performance with different settings directly. To address this, quasi-steady state measurement points were determined based on the time-varying data. The refrigerant temperature at the outlet of the LH-TES (T_{7a}) was used as criterium to determine the quasi-steady state points in periods where other inputs were kept constant. The procedure is illustrated in Figure 3.

https://doi.org/10.52202/077185-0049

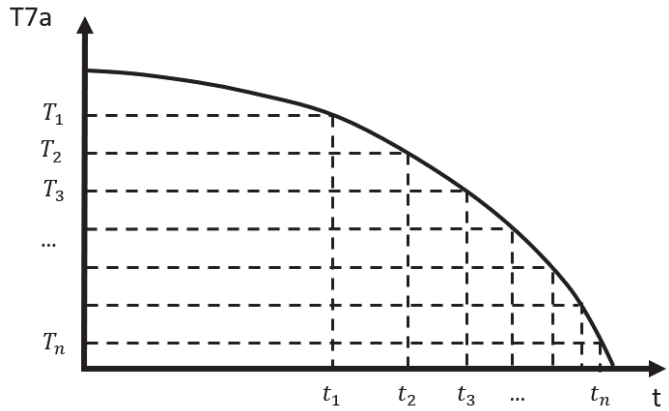

Figure 3. Schematic representation of procedure used to determine quasi-steady state measurement points.

Keeping all control parameters constant, the outlet temperature of the LH-TES (T_{7a}) is continuously decreasing (except for measurement noise) due to the heat transfer characteristics of a PCM based LH-TES heat exchanger. The time it takes for this outlet temperature to drop to a certain reference value can thus be determined uniquely. The reference temperatures were determined in 2 °C intervals. Identical reference temperatures were used for each experiment to allow comparison. These intervals are large enough compared to the measurement uncertainty and result in decent time intervals for averaging, yet they are small enough to track the influence of the heat source temperature on the ORC performance. The experiment durations t_x corresponding to the reference outlet temperatures T_x were determined for all periods with constant input parameters. For each 2 °C temperature interval $[T_i, T_{i+1}]$ (y-axis), the corresponding time interval $[t_i, t_{i+1}]$ (x-axis) can thus be determined. All measured values were then averaged in the time interval $[t_i, t_{i+1}]$ to obtain the quasi-steady state values corresponding to the temperature interval $[T_i, T_{i+1}]$. Different tests can then be compared by comparing these steady-state values in corresponding temperature intervals.

3 RESULTS & DISCUSSION

3.1 Transient evolution of the LH-TES outlet temperature

The refrigerant temperature at the LH-TES outlet (T_{7a}) during the first test (SH-TES 135 °C - $SC_{ev,in}$ 5-10 °C) is show in Figure 4. After the initial start-up phase (0 to 0.5 h), the refrigerant mass flow rate and expander speed were kept constant. The LH-TES outlet temperature dropped during nominal operation (0.5 to 3.38 h) due to the decreasing SOC of the LH-TES. The cycle behavior is thus inherently transient, even when the controllable inputs are kept constant. This transient behavior explains the need to derive quasi-steady measurement points when comparing different experiments. The decreasing outlet temperature results in a decreasing superheat at the expander inlet (point 7 in Figure 2). The shutdown procedure was initiated when this superheat became too low to avoid damaging the expander.

https://doi.org/10.52202/077185-0049

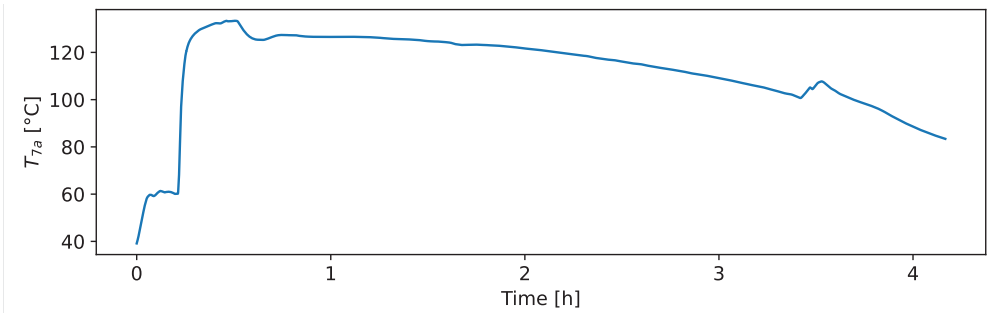

Figure 4: Transient evolution of the refrigerant temperature at the LH-TES outlet (T_{7a}).

3.2 Heat input

The heat input to the system in different quasi-steady intervals during nominal operation is shown in Figure 5. As the LH-TES outlet temperature (T_{7a}) is continuously decreasing, the figures should be interpreted chronologically from right to left. The influence of the SH-TES temperature can be assessed by comparing the black and blue measurements. Comparison of the blue and red measurements allows to study the influence of the subcooling at the LH-TES inlet (point 4 in Figure 2).

Figure 5 (a) illustrates that the total heat input to the system does not depend on the studied case. In the base case (SH-TES 135 °C - $SC_{ev,in}$ 5-10 °C), the total heat input to the system dropped from 85 kW_{th} to 75 kW_{th} during 2 h 38 min of stable operation, although the input parameters were kept constant. Similarly, the total heat input dropped from 84.1 to 76.2 kW_{th} in 2 h 38 min at lower SH-TES temperature. Increasing the subcooling at the LH-TES inlet shortened the test duration, as the total heat input dropped from 84.7 to 76.1 kW_{th} in 1 h 53 min. This difference can be explained by the division of the heat input over both thermal storage systems, as shown in Figure 5 (b). When only reducing the SH-TES temperature, the share of heat provided by the LH-TES remains constant. As the SH-TES temperature was sufficiently higher than the evaporation temperature in both cases, the subcooling could be kept in the desired range of 5-10 °C by increasing the water mass flow rate (Figure 5 (c)). However, due to the higher SH-TES water mass flow rate the SH-TES hot tank got depleted faster. In the current setup, the capacity of the LH-TES was the limiting factor and this faster depletion does not reflect in a shorter test duration. Increasing the subcooling at the LH-TES inlet increased the fraction of the heat input provided by the LH-TES. The LH-TES was thus depleted faster, which explains the shorter test duration. On the other hand, the water mass flow rate from the SH-TES was lower if a higher subcooling was used (for similar SH-TES temperature). This means that the SH-TES depletion rate was lower. Changing the subcooling thus allows shifting the main energy input and prolong the operation depending on the SOC of both storage components. As illustrated in Figure 5 (f), the superheat at the LH-TES outlet remained stable in all cases. Given the limited influence on the ORC operation, the division of the heat input between the SH-TES and LH-TES can thus be optimized.

https://doi.org/10.52202/077185-0049

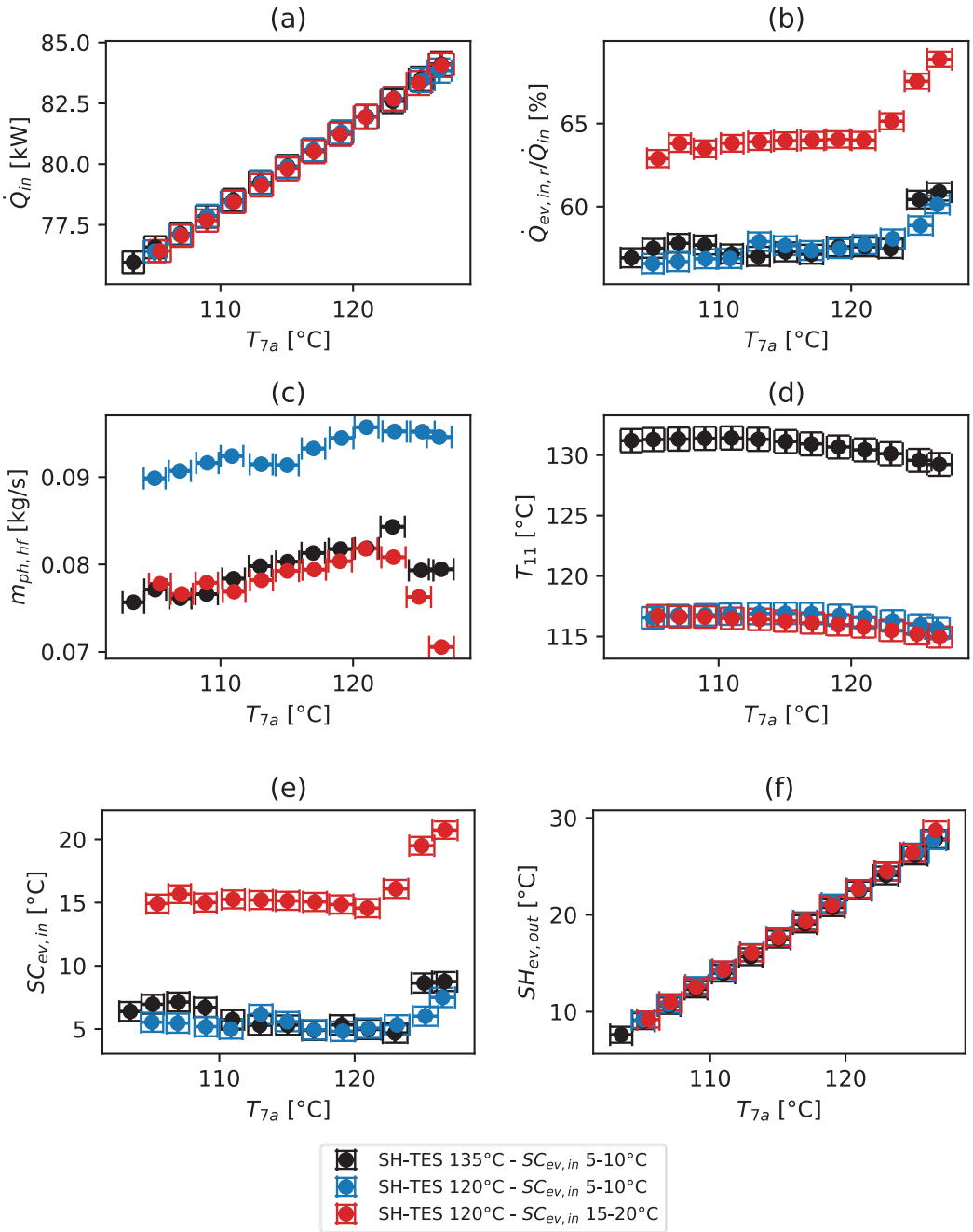

Figure 5: Overview of the heat input to the ORC.

3.3 Expander operation

The similar heat input to the system results in similar operating conditions for the expander as illustrated in Figure 6.

In all cases, the reduced heat input and reduced LH-TES outlet temperature (T_{7a}) result in a significant reduction in expander inlet pressure p_{7b} (Figure 6 (a)). This can be explained by the characteristics of the volumetric pump and expander. The volumetric pump imposes a constant volumetric flow rate, which corresponds to a rather constant mass flow rate due to its liquid inlet (and thus very small suction

https://doi.org/10.52202/077185-0049

density variations). For the expander on the other hand, the change in gas suction density has an important effect on the resulting mass flow rate. Assuming that the expander works at constant speed and that the small variation in volumetric efficiency η_{vol} shown in Figure 6 (d) can be neglected, it follows from the mass balance that the density at the expander inlet should remain constant. Therefore, as a decreasing temperature at constant pressure would increase the density, the evaporator pressure has to drop to keep the density constant. As shown in Figure 6 (b), the decreased expander inlet pressure results in a decreased expander power $\dot{W}_{exp}$. For the base experiment, a power reduction of 0.764 kW was observed, which corresponds to 12.5 % of the initial power output. Remark that the decreasing trend of expander power with decreasing LH-TES temperature is not followed at the highest LH-TES outlet temperatures. These measurements correspond with the start of the test. At this moment, the metal casing of the expander was still gradually heating up, which required part of the energy supplied. This results in lower power production. Comparing the corresponding steady operating points between the base test and the test with reduced SH-TES temperature, the maximum difference is 0.15 kW and the average difference is 0.09 kW. The influence of the subcooling at the LH-TES inlet is even smaller, with a maximum absolute and average deviation for corresponding measurements of 0.084 and 0.043 kW respectively, which corresponds to a maximum and average relative deviation of 1.6 and 0.76 %. The expander isentropic efficiency η_{exp} shows a slighly decreasing trend with decreasing LH-TES outlet temperature, but this difference is not significant. Finally, the volumetric efficiency η_{vol} also shows a decreasing trend, but the difference is small. The SH-TES temperature and subcooling at the LH-TES inlet have no significant effect on both efficiencies.

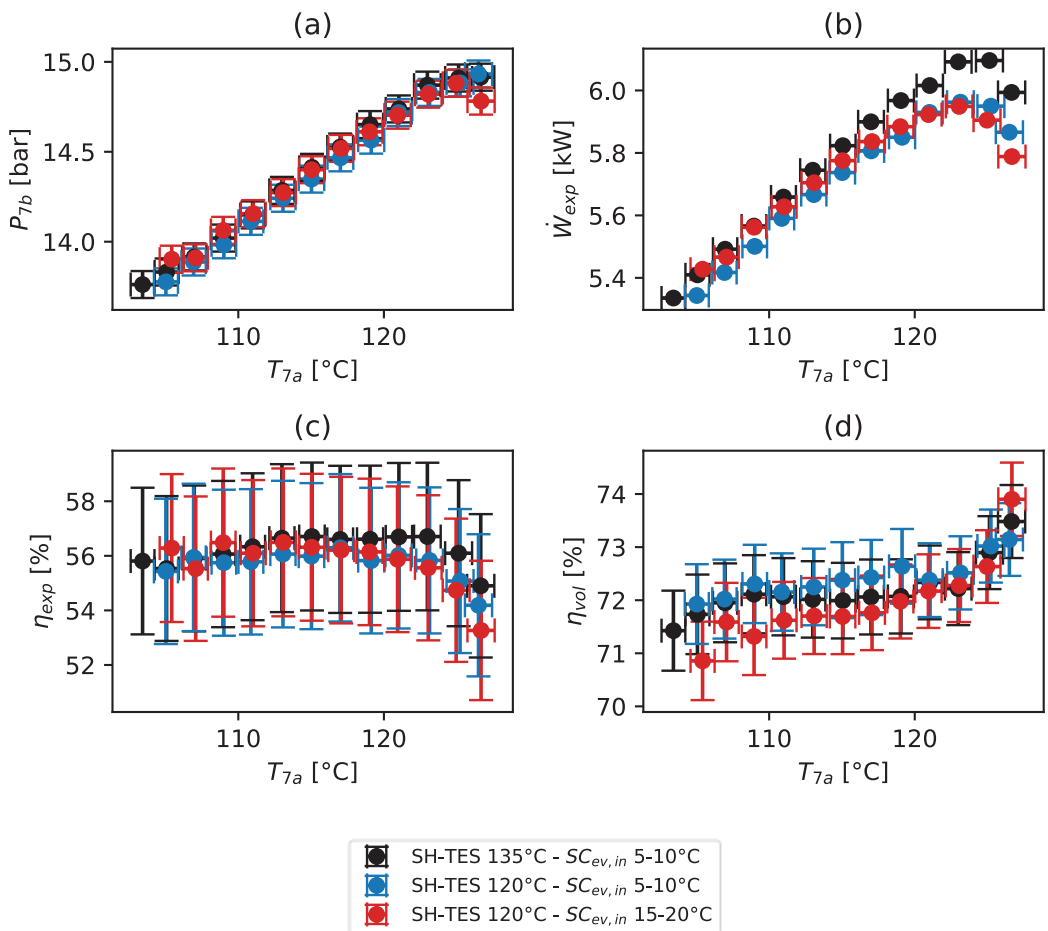

Figure 6: Influence of LH-TES outlet temperature on the expander operating conditions.

https://doi.org/10.52202/077185-0049

3.4 Cycle performance

The evolution of the cycle efficiency and FoC is shown in Figure 7. As discussed before, the decreasing LH-TES outlet temperature reflects the reducing heat input to the system. Simultaneously, the expander power output decreases. From Figure 7 (a), it can be seen that the cycle efficiency drops with decreasing LH-TES outlet temperature, meaning that the reduction of electrical power output is dominant compared to the reduced heat input. Given the similar heat input and expander power, the cycle efficiency is similar for all tests. The maximum and average efficiency difference between the base test and the reduced SH-TES inlet temperature test equal 0.17 % and 0.1 % in corresponding temperature intervals respectively. Although small, these differences are experimentally significant in the current analysis because the error on the electrical power measurement is assumed negligible. Comparing both tests with a SH-TES temperature of 120 °C but different subcooling, the maximum absolute and average difference between both tests were 0.11 and 0.06 % in the corresponding temperature intervals. The maximum differences occur at the highest LH-TES temperature. This can be explained mainly by the duration of the start-up procedure, causing slightly more or less energy used to heat up setup components at the time of measurement. In Figure 7(b), it can be seen that the FoC increases despite the reducing cycle efficiency with reducing LH-TES temperature. Relatively, the Carnot efficiency thus drops more with the reducing LH-TES outlet temperature than the measured cycle efficiency. However, this trend is similar for all tests compared. Overall, it can thus be concluded that the SH-TES inlet temperature (within the studied temperature range) and degree of subcooling have almost no influence on the cycle efficiency.

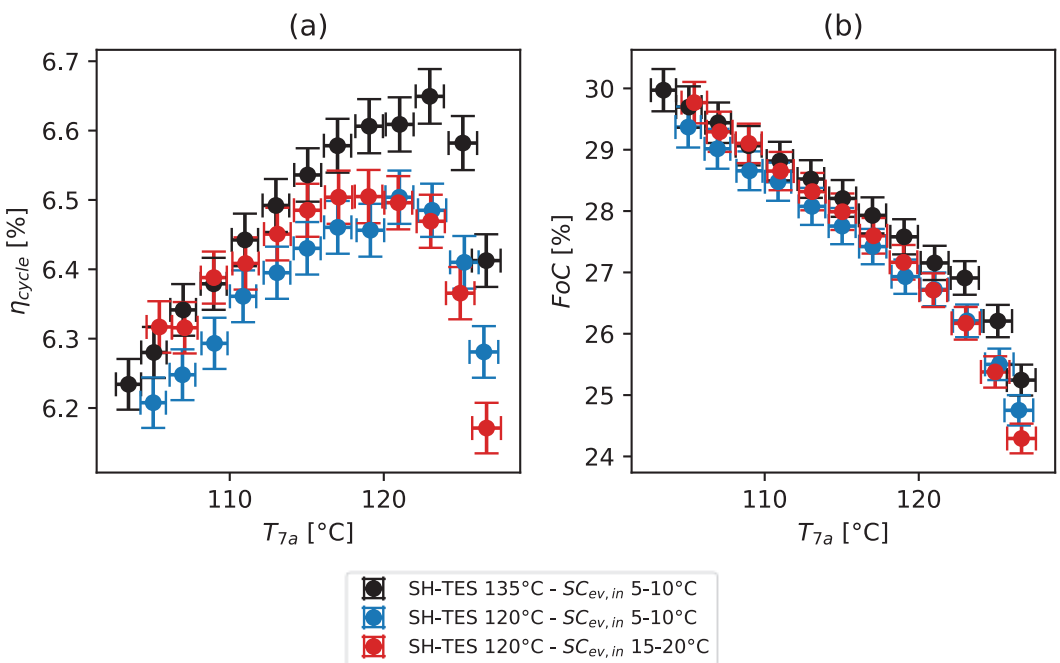

Figure 7: Influence of LH-TES outlet temperature on the cycle performance.

4 CONCLUSIONS

A first of its kind CHEST prototype was developed within the Horizon2020 CHESTER project. The storage system of this prototype consists of a sensible and latent heat thermal storage system. An organic Rankine cycle was used during discharging. Successful operation of the ORC within the full prototype was demonstrated. The results show that the thermal efficiency of the ORC is not sensitive to the actual distribution of the heat input, as long as the heat input to the system can be sustained. This means that the SH-TES temperature and subcooling at the LH-TES inlet (and thus division of the heat input over

https://doi.org/10.52202/077185-0049

both thermal storage systems) can be optimized to extend operation as long as possible. This is especially important as the depletion of the LH-TES has been found to have an influence on the maximal power production and operating duration. The ORC itself thus supports a high flexibility towards different residual heat source temperatures and storage systems, making it applicable in a wide range of operating scenarios.

NOMENCLATURE

CHEST	compressed heat energy storage	(–)
EES	electrical energy storage	(–)
FF	filling factor	(–)
FoC	fraction of Carnot	(–)
HP	heat pump	(–)
HT	high temperature	(–)
LH	latent heat	(–)
ORC	organic Rankine cycle	(–)
PCM	phase change material	(–)
$\dot{Q}$	heat flow rate	(W)
SC	subcooling	(K)
SH	sensible heat / superheat	(– / K)
SOC	state-of-charge	(–)
TES	thermal energy storage	(–)
VRE	variable renewable energy	(–)

Subscript

cf	cooling fluid
cond	condenser
ev	evaporator
exp	expander
hf	heating fluid
in	inlet
is	isentropic
net	netto
out	outlet
ph	preheater
r	refrigerant
th	thermal
vol	volumetric

Greek symbols

η	efficiency

REFERENCES

CHESTER. 2023. Compressed Heat Energy Storage for Energy from Renewable sources (CHESTER). Retrieved 02/02/2024 from https://www.chester-project.eu/

Couvreur, K., Tassenoy, R., van Heule, X., De Paepe, M., & Lecompte, S., 2022, Experimental and numerical analysis of variable volume ratio as additional optimization parameter in organic Rankine cycle expanders, *Applied Thermal Engineering*, *216*: 119007.

De Paepe, M., Lecompte, S., & Pillai, A. 2019. D3.4 Detailed design of the ORC laboratory prototype.

Dumont, O., Frate, G. F., Pillai, A., Lecompte, S., De paepe, M., & Lemort, V., 2020, Carnot battery technology: A state-of-the-art review, *Journal of Energy Storage*, *32*: 101756.

Enerdata. 2023. World Energy & Climate Statistics - Yearbook 2023 - Renewable in electricity production share. Retrieved 25/09/2023 from https://yearbook.enerdata.net/renewables/renewable-in-electricity-production-share.html

https://doi.org/10.52202/077185-0049

European Commission , Directorate-General for Energy , Andrey, C., Berberi, P., & Nuffel, L. 2020. Study on energy storage: contribution to the security of the electricity supply in Europe. https://data.europa.eu/doi/10.2833/077257

Hassan, A., Corberán, J.-M., & Sanchez, V. 2019. D3.2 Detailed Design of the High Temperature Heat Pump Laboratory Prototype.

Hassan, A. H., Corberán, J. M., Ramirez, M., Trebilcock-Kelly, F., & Payá, J., 2022, A high-temperature heat pump for compressed heat energy storage applications: Design, modeling, and performance, *Energy Reports*, *8*: p. 10833-10848: 10833.

Hassan, A. H., O'Donoghue, L., Sánchez-Canales, V., Corberán, J. M., Payá, J., & Jockenhöfer, H., 2020, Thermodynamic analysis of high-temperature pumped thermal energy storage systems: Refrigerant selection, performance and limitations, *Energy Reports*, *6*: p. 147-159: 147.

He, Y., Guo, S., Zhou, J., Song, G., Kurban, A., & Wang, H., 2022, The multi-stage framework for optimal sizing and operation of hybrid electrical-thermal energy storage system, *Energy*, *245*: 123248.

Jockenhöfer, H., Steinmann, W.-D., & Bauer, D., 2018, Detailed numerical investigation of a pumped thermal energy storage with low temperature heat integration, *Energy*, *145*: p. 665-676: 665.

Lund, R., 2021, Energy System Benefits of Combined Electricity and Thermal Storage Integrated with District Heating, *International Journal of Sustainable Energy Planning and Management*, *31*: p. 23-38: 23.

Lund, R., Komoszynska, M., Stark, S., & Herrero, J. P. 2021. D6.4 Market technological potential.

Novotny, V., Basta, V., Smola, P., & Spale, J., 2022, Review of Carnot Battery Technology Commercial Development, *Energies*, *15*(2): 647.

Sánchez-Canales, V., Payá, J., Corberán, J. M., & Hassan, A. H., 2020, Dynamic Modelling and Techno-Economic Assessment of a Compressed Heat Energy Storage System: Application in a 26-MW Wind Farm in Spain, *Energies*, *13*(18): 4739.

Stark, S., & Bestenlehner, D. 2021. D4.5 Full scale CHEST system optimization and techno-economic assessment.

Steinmann, W. D., 2014, The CHEST (Compressed Heat Energy STorage) concept for facility scale thermo mechanical energy storage, *Energy*, *69*: p. 543-552: 543.

Theologou, K., Johnson, M., Tombrink, J., Corrales Ciganda, J. L., Trebilcock, F. T., Couvreur, K., Tassenoy, R., & Lecompte, S., 2024, CHESTER: Experimental prototype of a compressed heat energy storage and management system for energy from renewable sources, *Energy Conversion and Management*, *311*: 118519.

Vaz, D., & Carrera, A. 2021. D4.6 Smart Energy Management System for efficient operation of the CHEST system.

Vecchi, A., Knobloch, K., Liang, T., Kildahl, H., Sciacovelli, A., Engelbrecht, K., Li, Y., & Ding, Y., 2022, Carnot Battery development: A review on system performance, applications and commercial state-of-the-art, *Journal of Energy Storage*, *55*: 105782.

Weller, T., Jockenhöfer, H., Fiss, M., & Bauer, D. 2019. D3.3 Detailed design of the high temperature TES laboratory prototype.

ACKNOWLEDGEMENT

This work has been partially funded by the grant agreement No. 764042 (CHESTER project) of the European Union's Horizon 2020 research and innovation program. This support is gratefully acknowledged.

https://doi.org/10.52202/077185-0049